Spatio-temporal structure and emission of a large plasmoid in atmosphere

R Friedl[1], U Fantz[1,2], I. Pilottek[1], D. Schmid[1] and S. Steibel[1]

[1] AG Experimentelle Plasmaphysik, Universität Augsburg, 86135 Augsburg
[2] Max-Planck-Institut für Plasmaphysik, Boltzmannstr. 2, 85748 Garching

E-mail: `roland.friedl@physik.uni-augsburg.de`

Abstract. Atmospheric plasmoids with 20–30 cm diameter are generated via a high-voltage discharge above a water surface. They ascent in the ambient air and exist autonomously for several hundreds of milliseconds. The plasma processes leading to an emission of visible light for more than 350 ms after detachment from the energy supply are still unknown. Visual and spectroscopic high-speed diagnostics with spacial resolution are thus applied. It is shown for the first time that the free-floating body turns to a torus ring to the end of its lifetime which ascends in air up to more than 1.5 m and radiates longer than 1.5 s in the infrared spectral range, only limited by the structural circumstances in the laboratory. Vortex formation is thus endorsed as being responsible for the structural integrity of the plasma during the autonomous phase. Emission in the optical spectral range (UV-NIR) is limited to the first 500 ms and is governed by radiation from the tap water contents without influx of ambient air into the plasma. The OH A-X transition is the most intense emission during the entire visible evolution of the plasmoid. Atomic hydrogen emission is observed only during the first 100 ms close to the central electrode (CE) and is highly dynamic, while emission from dissolved salts is detected during the later evolution but is mostly overlaid by a continuum radiation which is clearly non-thermal. Using the omnipresent OH emission, the optical emission profile of the main plasmoid is shown to be broad in the center and is rotationally symmetric. The radiated energy from the OH radical integrated over the entire plasmoid evolution is less than 100 J, which is about 3 % of the total energy dissipated into the plasma. Emission from dissolved sodium is used to track the plasma channel, which connects the main plasmoid to the CE, during its ascension after energy shut-down giving a 4-fold ascension velocity compared to the main plasmoid.

1. Introduction

Laboratory-generated atmospheric plasmoids, i.e. a nearly ball-shaped plasma ascending from a water surface, attracted interest in the last decades due to their similarity to the ball lightning phenomenon (see [1] and references therein). The experimental setup goes back to the one presented by Shabanov et al. in 2001 [2]: A tip electrode and a ring or plate electrode are immersed in a vessel of some liters of aqueous solution, where the tip electrode slightly protrudes the water surface. Applying high voltage to the electrodes generates a plasma above the water surface which rises in ambient atmosphere due to buoyancy. A plasma ball of several tens of centimeters is formed which ascends with several m/s. After a certain time the connection to the tip electrode is capped (either due to the progressed ascension of the plasmoid or due to opening a switch) and the plasmoid enters an autonomous phase during which it exists without external energy supply. This phase can last up to several hundreds of milliseconds.

Since then, several laboratories around the world have recreated the setup and applied numerous diagnostics to analyze the visual, electrical, physical and chemical properties [3–17]. While high-speed videography is used in all of them and the electrical characteristic is monitored at least in most of them [4, 6–12, 14–17], specific diagnostics like electrical probes [4, 6, 7], photo sensors [4, 6, 11], thermal sensors [7], optical and infrared emission spectroscopy [5, 7, 10, 13, 16] and even sophisticated methods as Fourier-transform infrared (FTIR) absorption spectroscopy [11] and mass spectrometry [14] have already revealed several specific characteristics of this kind of discharge.

However, the formation of the observed autonomous phase and its long-time existence still bare many questions. The structural stability is believed to be correlated to the formation of a vortex ring [11,17–19], while the background of the persistent luminosity is approached by optical emission spectroscopy. Here, spatio-temporal investigations can give valuable insight into the occurring plasma processes. Typically, spectrometers are used with one line of sight (LOS) [5, 7, 10, 13] which have a time resolution between 50 and 100 ms. For the highly dynamic system of the atmospheric plasmoid, higher temporal resolution together with several LOS at the same time would, however, be highly desirable.

In continuation of the investigations in [12,13,15], this paper constitutes a summary of the findings over the last years and sets them in context to published work in this field. It is a first step towards a full spatio-temporal characterization of the plasmoid emission. Photodiodes are applied in order to give a high temporal resolution (ms range), while spectral resolution is obtained by the application of interference filters. Using several diodes simultaneously, aligned vertically or horizontally, a spatial resolution is obtained and a wide range of intensities is covered (more than 4 orders of magnitude). Absolute intensities are obtained by calibration against an Ulbricht sphere, among others. Furthermore, high-speed videography is used with and without the application of interference filters to get the full spatio-temporal emission, yet without absolute intensity numbers. These studies are the basis for a detailed analysis of specific radiating plasma constituents with finely timed high-resolution spectroscopy.

2. Generation of the plasmoid

The experimental setup is shown in figure 1 [12, 15]. The main component is the acrylic glass vessel filled with about 6 liters of tap water. A copper plate serves as anode and is immersed in the water tank 15 cm below the water surface. The grounded cathode is a tungsten rod (3 mm diameter, 16 cm length) in the center of the vessel, fed through a hole of 25 mm in the anode plate. It is surrounded by ceramics to insulate it from the water reservoir and a further insulator is used in between to center the tungsten rod in the ceramic tube (see the magnification inset in figure 1). The tip of the tungsten rod is at the water surface serving as the central electrode (CE). The ceramic tube protrudes above the water surface, such that a small volume of water (≈ 1 ml) is separated from the rest. Watertight connections from the bottom of the vessel for both electrodes prevent any influence of possible asymmetric potential distributions at the water surface or within the vessel.

A bank of 18 capacitors with $137.5\,\mu F$ capacitance each (stackable for a total capacitance between $0.55\,mF$ and $2.5\,mF$) is charged by a high-voltage power supply up to $6\,kV$. The main system trigger closes a pneumatic switch and the voltage is applied to the electrodes. This leads to breakdown between the CE and the water surface and within $100\,ms$ a ball-shaped plasmoid of 20–30 cm diameter is formed ascending in the ambient air. About $150\,ms$ after breakdown the switch is opened and the autonomous phase starts. The detailed description of the starting sequence and the temporal evolution is given in section 3.

2.1. General diagnostics

Current and voltage measurements as well as the photodiode diagnostics (described in detail in section 5) are started automatically with the main system trigger. Videography is started manually beforehand and is performed using two cameras. The high-speed camera Casio Exilim EX-F1 (denoted as camera 1) can
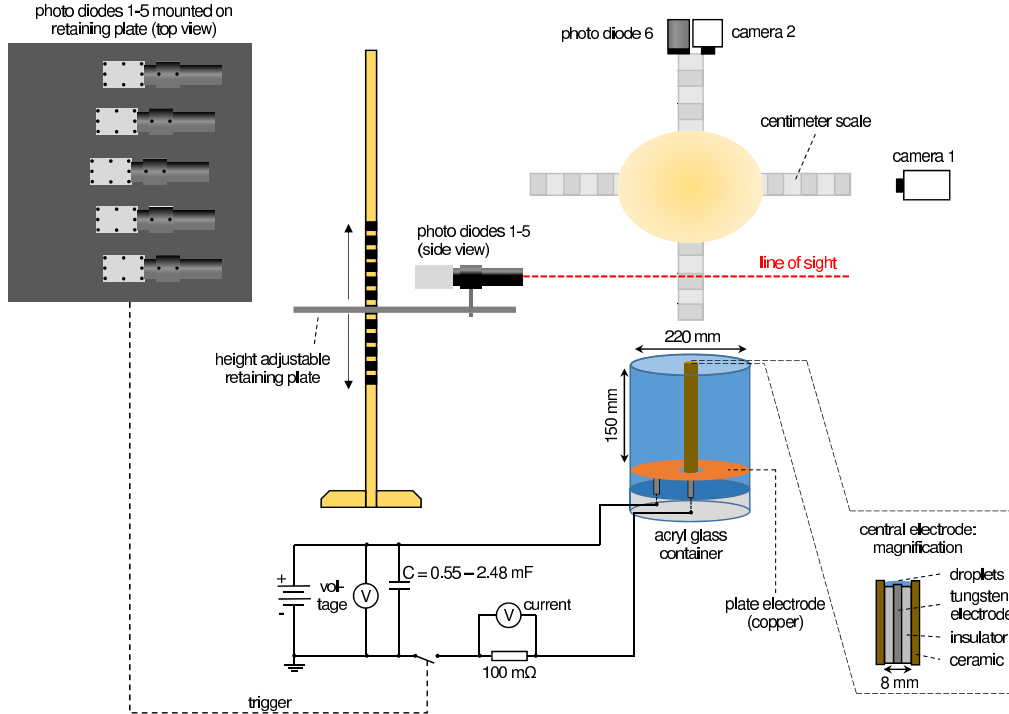
Figure 1. Experimental setup for the generation of atmospheric plasmoids including the diagnostics.

be used with two different speed settings: 600 frames per second (fps) at a resolution of 432×192 pixels and 1200 fps at 336×96 pixels. Typically, wide shot recordings of the entire plasmoid evolution are taken with 600 fps, while special close-up recordings focusing on the early behavior at the central electrode are taken with 1200 fps (see figure 2). Furthermore, the camera can be applied to take high resolution photos as shown in [13] for instance. For some of the measurements also a GoPro Hero 4 Black Edition is used from above the setup (camera 2). It has a frame rate of 240 fps with a resolution of 848×480 pixels. The infrared camera used for the recordings of figure 3 has a resolution of 640×480 and a frame rate of 30 fps. Measuring tapes with a scale of 2 cm behind the setup as well as beneath the vessel (see figure 2) are used for geometrical analyses of the videos, as shown in detail in [15].

In order to bring the manually initiated cameras in correlation with the absolute time given by the system trigger, an LED array is available: on triggering, it starts with a delay of below 1 ms and lights up one of nine blue LEDs every ≈ 9 ms. Typically, the LED array is positioned in the field of view of camera 1 in the wide shot configuration. Due to the stepwise activation of the LEDs, the time between system trigger initiation and first light emission from the discharge can be given to an accuracy determined only by the frame rate, i. e. to ± 1.67 ms at 600 fps. Operation of the LED array

can be seen in the side view video of figure 2 in the supplemental material (link?). For the frames taken for figure 2 this part of the video is cut due to reasons of space.

Furthermore, a handheld conductivity meter, Extech EC400, is available to measure water temperature and conductivity before each discharge.

2.2. Standard conditions

Most of the measurements presented herein were taken under the following parameters representing the 'standard conditions':

voltage	4.9 kV
capacitance	2.5 mF
water temperature	20.5 ± 2.5 °C
conductivity	530 ± 30 µS/cm

Conditions differing from the above mentioned are denoted explicitly.

3. Temporal behavior, indications for vortex ring formation and measures of the lifetime

On triggering, the pneumatic switch closes within ≈ 15–35 ms after which the high voltage is applied to the electrodes and the breakdown occurs. This is accompanied by the immediate onset of the discharge
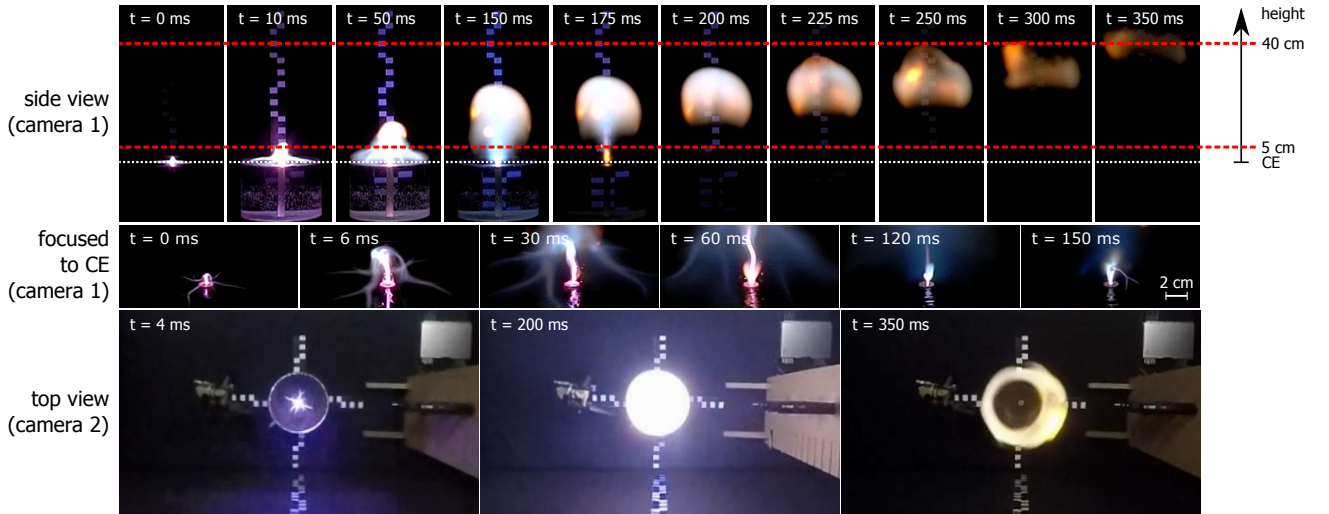
Figure 2. Evolution of the plasmoid discharge for standard conditions, seen from different angles and with different frame rates: side view (camera 1) at 600 fps, focused to CE (camera 1) at 1200 fps, top view (camera 2) at 240 fps. Side and top view frames belong to the same discharge, frames focused to the CE are from a discharge with identical external parameters. The videos can be found in the supplemental material (link?). For the side view frames, the levels of the central electrode (CE) as well as of 5 and 40 cm distance above the water surface are given for height correlations of the following results.

current (see also figure 4) and the first light emission is recorded with the cameras. The coincidence of onset of current flow and light emission could be accurately determined with help of the LED array described above. For the measurements presented here, the time $t = 0$ is thus set at the point of first increase of current and will be referred to as 'discharge ignition'. The switch is opened about 175 ms after the trigger time. Taking the delay of closing the switch into account, the typical energy supply time is thus 150 ± 10 ms. The temporal evolution of the plasmoid in standard conditions is shown in figure 2 for different fields of view. The respective full video files can be found in the supplemental material.

Breakdown occurs at $t = 0$ and streamer-like plasma filaments develop from the CE over the protrusion of the insulation ceramics. The filaments connect the CE to the water surface and increase rapidly in length over the water surface. The water in the small reservoir at the CE rapidly heats up and a jet emerges which drives the water to splash out of the CE (see focused frame at $t = 6$ ms). This can be seen with much more dynamic in [17] for instance. The jet increases in length and at its top a spherical plasma evolves. A high-resolution photo of this phase can be found in [13], where also waves can be seen driven by the streamer heads (in [20] this phenomenon is described as electrohydrodynamic water-surface perturbations). At $t = 50$ ms the spherical dome can be recognized in the frames presented here. The electrical connection between CE and water surface is still constituted by plasma filaments which start at the lower end of the jet connected to the water surface

close to the CE. With time they rise upwards along the jet while they simultaneously increase in length over the water surface. At some point in time the conductivity through the plasma channel gets too low due to the increasing length and the filament vanishes while a new one develops from the lower end. This repetitive behavior is described in detail in [17] and can be seen in the focused video file. In figure 2 at $t = 150$ ms one of these filaments can be seen directly after emergence. The lower exposure in this video (1200 fps vs. 600 fps) gives the impression, the plasmoid would already be detached from the CE. However, in the side view video it is obvious that the connection to the central electrode still exists. In this phase the three main components of the phenomenon can be recognized: the ball shape of the main plasmoid, the central jet connecting the plasmoid to the CE and the streamers above the water surface which can appear as a 'plasma cloud' depending on the exposure time of the applied camera and the associated blur effect.

Shortly after the frame at $t = 150$ ms the switch opens and the connection to the capacitors is capped, i.e. no further energy can be supplied to the system and the autonomous phase starts. The jet and the streamers vanish immediately and within ≈ 35 ms the remaining plasma channel and the 'cloud' are completely retracted towards the main plasmoid. The frames at $t = 200$ ms give the free floating ball-shaped plasmoid with a diameter of 25 ± 2 cm in side as well as top view.
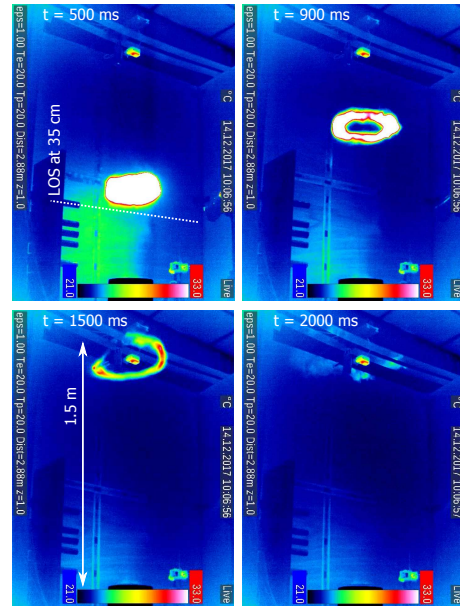
In the following the brightness is low enough to discern a relatively high toroidal dynamic of the system (see video in the supplemental material). This dynamic

leads to the formation of a torus ring, which can nicely be seen in the top view frame at $t = 350$ ms. In the center of the ring, no optical emission from the plasmoid but instead the central electrode beneath it can be seen, indicating that there is no plasma. This observation is consistent with the formation of a vortex ring, which was mentioned first by Versteegh [18] and discussed in detail by Kalafat [19].

Formation of a vortex requires 'ejecting' a medium into another medium initially at rest. For the situation of an atmospheric plasmoid this would be the plasma emerging from the central electrode into the surrounding ambient air. A radial velocity gradient of the ejecting medium together with a distinct friction between the two media leads to deflection perpendicular to the propagation direction and thus to a rotational movement of the ejecting medium. This results in the distinctive vortex ring or torus structure. Such vortices can easily look like spheroids or ellipsoids from the outside as is shwon in [21] in figure 2 (b) for instance, which explains the appearance of the plasmoid as a 'plasma ball'. Due to the poloidal rotation of the torus a pressure drop underneath the vortex develops which drives the surrounding medium to be entrained into the vortex leading to non-mixing layers of both media (see for example [22]). It can thus be expected that the plasmoid itself consists of layered structures of plasma and non-ionized ambient air.

This discussion gives the strong indication that the structural stability of atmospheric plasmoids is correlated to the formation of a stable vortex already from the very beginning. It's internal structure is, however, only revealed after disconnecting the power supply, since from this moment on no further plasma is ejected to the center of the plasmoid and the torus structure can be recognized. The idea of a vortex or at least a poloidal rotation is already mentioned in [7,17] and in [11] the vortex structure was already indicated by use of schlieren videography. The recordings from above the experiment, i.e. with a line of sight parallel to the propagation axis, made it now possible to visualize for the first time the actual toroidal shape of the plasmoid.

The total visual lifetime of the plasmoid is determined via video analysis and given as the time at which no emission is detected anymore, i.e. when the brightness reflects the background noise and the frame's appearance is completely dark. The contrast of the frames is increased for this purpose (see figure 8 for instance). For the side view video, 465 ms are thus determined, while in the top view video with increased exposure and strong oversaturation to the beginning of the discharge the visual lifetime is 775 ms. This deviation of 'lifetimes' is even more severe when varying the observed spectral range. Figure 3 shows
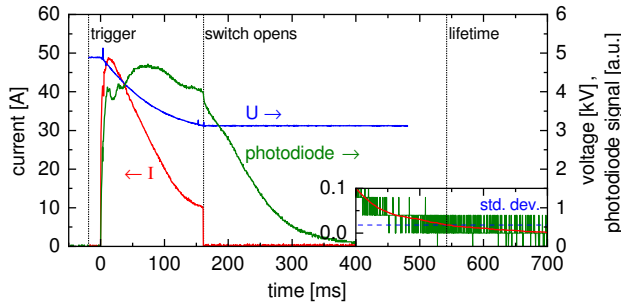

Figure 3. Late evolution period of the plasmoid for standard conditions taken by IR videography at 30 fps. The warm electronics of camera 2 can be seen at the ceiling of the laboratory. The video can be found in the supplemental material (link?). For height correlations the LOS at 35 cm above the water surface is highlighted and the distance of the upper suspensions is given. Note: The temperature scale cannot be used to assess the plasmoids temperature, since its emission is strongly non-thermal (see figure 5).

frames from IR videography at 30 fps. From this angle and due to overexposure the plasmoid at $t = 500$ ms still looks ellipsoidal. But at a later stage the toroidal structure can be seen also here. At $t = 1.5$ s the plasmoid reaches the upper suspensions 1.5 m above the CE where camera 2 is mounted. Due to the impact of the plasmoid torus the temperature of the upper structures increases by some degrees as can be seen at $t = 2$ s. Hence, the vortex ring itself is very stable and its lifetime is actually only limited by obstacles in its way of ascension, even if it is no longer radiating in the visible spectral range.

These recordings impressively confirm that a measure of the lifetime via videos strongly depends on the detector settings (wavelength-dependent sensitivity, shutter time etc.) and in the end to a possibly subjective impression about the end of light emission. In order to establish a fully reproducible lifetime diagnostic, we have implemented a simple technique based on a photodiode mounted at the ceiling of the laboratory (diode 6 in figure 1). It records the integral plasmoid emission in the wavelength range 185–1100 nm (chip's sensitivity). Results from this diode together with electrical waveforms from the discharge of figure 2 are given in figure 4.

After the system trigger the switch takes 19 ms to close and plasma ignition starts at $t = 0$. Within

Figure 4. Current, voltage and diode (nr. 6) signals for the discharge shown in figure 2 (side and top view). The inset shows the lifetime analysis via the photodiode signal (x-axis is identical, y-axis is scaled): the digital noise to the end is averaged and the standard deviation is taken as threshold.

12 ms the discharge current I reaches its maximum of 49 A and decreases afterwards to 10 A before the switch is opened at 160 ms. Due to the discharging current the capacitor voltage U decreases monotonically from initially 4.9 kV to 3.1 kV and the maximum dissipated power is about 227 kW. The resistance R_{water} of the water reservoir, derived by the minimum of the U/I-curve after [12], is at 95 Ω and the total dissipated energy $E = \int U \times I\,\mathrm{d}t$ is 17.6 kJ. After [15] the energy delivered to the plasma is thus $E_{plasma} = E - \int R_{water} \times I^2\,\mathrm{d}t = 3.6$ kJ, while the remaining energy (14 kJ) is dissipated into the 6-liter-reservoir, slightly heating the water with each discharge.

The signal from the photodiode shows a dynamic behavior to the beginning and a relatively broad maximum which is shifted by about 60 ms compared to the current maximum. After opening the switch the signal drops immediately, expectably due to the vanishing plasma jet, and it decays slowly afterwards. The end of this decay is determined by a threshold method (below 0.5 % of the maximal signal) and the evaluation gives the plasmoid's luminosity lifetime to about 542 ± 24 ms. Such a mathematical analysis is not prone to subjective impressions and can thus act as a robust diagnostic. However, one should keep in mind that the torus might leave the diode's field of view to the end of its life, as can be seen in figure 3, meaning that this value may still represent a lower limit.

4. Emission spectra and plasmoid composition

Figure 5 shows spectra taken with a survey spectrometer with a spectral resolution of about 1.4 nm at finely defined times ($\approx \pm 1$ ms) relative to discharge ignition. Time correlation was done by using a delay generator between the system trigger and the spectrometer shutter, and the absolute exposure time as well as any delays were determined with help of the LED array described in section 2.1. The spectra are each composed

of two recordings with central wavelengths at 377 nm and 657 nm and are calibrated for wavelength depending sensitivity using a D_2 arc lamp and an Ulbricht sphere. The line of sight (LOS) is positioned 15 cm above the water surface and the diameter of the LOS at the plasmoid's ascension axis is about 1.5 cm.

For the first (composed) spectrum the recording started already before discharge ignition and lasted until $t = 45.5$ ms, a time at which the plasmoid did not yet reach the line of sight (see camera frame right of the spectrum). This means the light recorded comes from reflections and thus, the relative emissivity depends on the wavelength-dependent reflectivity of the plasmoid surroundings (here: blackened wood wall). Nevertheless, in this phase of the plasmoid evolution only emission lines of atomic oxygen (777 nm) and hydrogen (Balmer series) can be observed.

The second spectrum represents the emission from the bulk plasmoid as it traverses the LOS. O and H are no longer observed, but the sodium resonance lines at 589 nm as well as lines from neutral and ionized calcium emerge. Furthermore, emission from calcium hydroxide CaOH can be seen (for a discussion on production channels see [7]) and the entire spectrum is underlaid by a broad continuum. Since the wavelength-dependent sensitivity of the spectroscopic system is considered, the spectral evolution of this continuum can be interpreted qualitatively and it turns out that it decreases monotonically with increasing wavelength. Hence, it strongly diverges from thermal radiation for which a maximum would be expected in the recorded spectral range. The origin of this continuum radiation is thus still object of investigations.

The most notable spectral component is, however, the emission from the hydroxyl radical OH $(A^2\Sigma \rightarrow X^2\Pi)$, which is orders of magnitude more intense than any other component in the spectrum. This is true for most of the passage time of the plasmoid through the LOS. Only to the end (last spectrum shown in figure 5) the emission from sodium intensifies to above the spectral emissivity of OH. In this phase even emission from potassium K can be seen at 766 and 770 nm. The integrated emissivity, however, is still dominated by OH.

Employing calibrated spectroscopy, it is thus reasserted (see [7] for instance) that the plasmoid's appearance is not due to thermal radiation, but due to a non-equilibrium plasma, which emerges from the tap water (H, O, OH) and the dissolved salts (Ca, Ca^+, CaOH, Na, K). No metallic lines from the electrodes are present since tungsten is used as CE and the water surrounding it might work as a cooling liquid. Furthermore, no emission from ambient air (N_2, NO) could be observed so far. However, this does not preclude that an air plasma might be involved
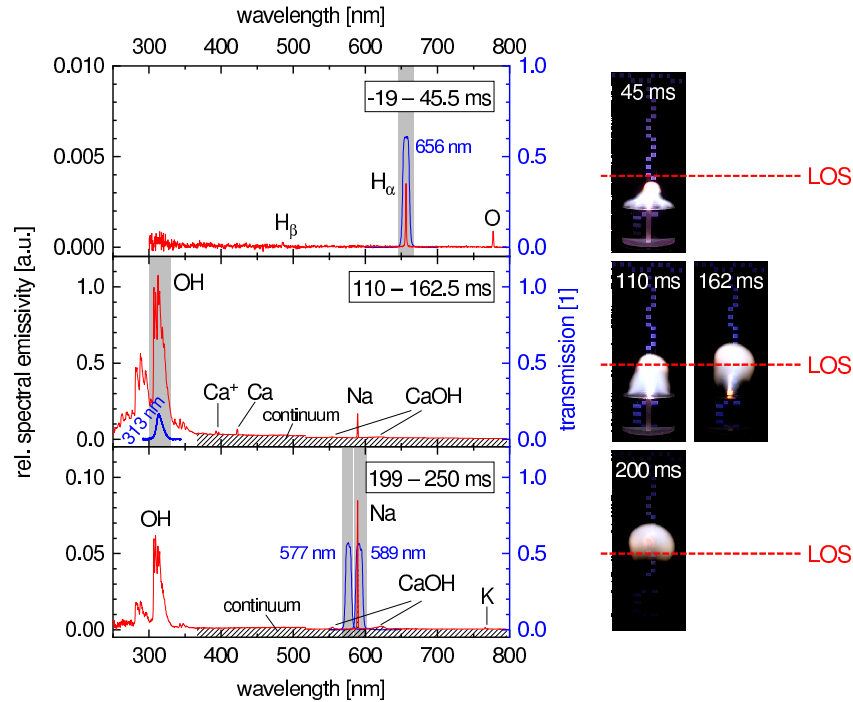
Figure 5. Spectra taken with a survey spectrometer at 15 cm height above the water surface for finely defined times (given as the interval during which the shutter collects light including opening and closing periods). Note the differing y-axis scaling. The main emission components are designated. Next to the graph photographs taken from high speed videography (camera 1) are shown, indicating the LOS in relation to the plasmoid for specific times. Transmission spectra for the applied interference filters for the photodiode diagnostic including the central transmission wavelengths are shown in blue with the right axis.

during the breakdown at the very beginning, or for the streamers above the water surface. Dubowsky et al. [14] have shown by mass spectrometry that products of air plasmas (NO_2^+, NO_3^+, and others) are present in the plasmoid 8 cm above the water surface. Furthermore, as hypothesized in [3, 6] and measured in [11, 14] the water vapor may build water clusters or condense as an aerosol within the plasmoid forming water droplets or bubbles [7, 17]. And due to vortex formation, non-mixing layered structures of a low-temperature water plasma and non-ionized ambient air might even exist (see section 3). The multitude of these findings illustrate that the plasmoid composition may be very complex. With the non-invasive optical emission spectroscopy at least the radiating part of the system is accessible without interfering the delicate gas dynamics.

5. Photodiode diagnostics

In order to gain insight into the highly dynamic behavior of the occurring plasma processes high-speed diagnostics are indispensable. Therefore, photodiodes are applied to monitor the spatio-temporal emission. Apart from the diode described above and used as a lifetime diagnostic (diode 6), five further photodiodes

(diodes 1–5 in figure 1) are used, each of them equipped with interference filters to monitor specific spectral components with high temporal resolution. The interference filters are chosen according to the optical emission spectra described above (central transmission wavelengths are given): the H_α line at 656 nm, the OH A-X emission at 313 nm, the sodium line at 589 nm and the unidentified continuum emission by a representative spectral range around 577 nm. Measured transmission curves of the respective interference filters are shown in figure 5 giving a transmission width of about 10 nm each. For the OH emission, about half of the emitted photon power of the A-X transition is detected through the filter.

5.1. Photodiode systems and calibration

The basic setup for the photodiode diagnostic is shown in figure 6. The main component is a silicon photodiode (1) of type Hamamatsu S1336-8BQ ($5.8 \times 5.8 \, mm^2$) with a spectral response between 190 and 1100 nm. The light exposing the diode chip is led through the interference filter (2, IF), both of them housed in a tube with an aperture stop (3) of 3 mm diameter at the entrance which limits the collection solid angle. Together with the first amplification stage
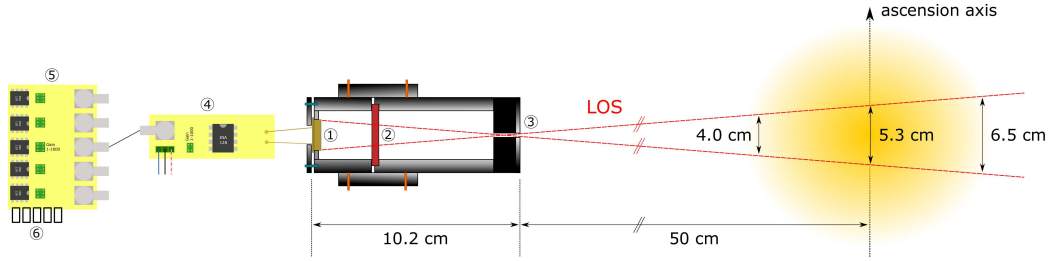
Figure 6. Sketch of the photodiode systems consisting of: 1. the silicon photodiode, 2. an interference filter, 3. an aperture stop, 4. first amplification, 5. second amplification, and 6. fiber optics connectors. The detection cone is illustrated (LOS) in relation to the plasmoid ascension axis.

(4) of a gain up to 10^3 this construct is called a 'photodiode system' (PD system) in the following. Five of these PD systems are connected to the power board (5) with a second variable amplification up to 10^3. The obtained signals are then transferred via fiber optics (6) out of the high-voltage area. Due to the back-and-forth conversion (electrical $\rightarrow$ optical $\rightarrow$ electrical) an additional amplification by a factor of 10 is obtained. Hence, the total amplification for a single PD system can be adapted between 10 and 10^7.

The PD systems have a temporal response of below 1 ms and the signals are recorded by a National Instruments break-out box with a sampling rate of 2 kHz. Intensity calibration of each combination of PD system and IF is performed by recording the emission from an absolutely calibrated Ulbricht sphere as secondary radiation standard. For calibration of the PD systems with the 313 nm filters, the OH emission from a low-temperature plasma is used: the signal from the PD system is compared to the emission measured by an absolutely calibrated spectrometer (which is in turn calibrated with an Ulbricht sphere and a D_2 arc lamp). As mentioned, not the entire wavelength range of the OH emission is detected and the missing amount of 50 % is not taken into account for this calibration.

5.2. Spatial arrangements

The PD systems' orifices are located 50 cm from the ascension axis of the plasmoid and the aperture stop determines the collection cone of the diode system: it has a diameter of around 4 cm at the near edge of the water vessel opening to about 6.5 cm at the far edge. Hence, in the plane of plasmoid ascension a spatial resolution of 5.3 cm is given. In order to limit the overlap of the observed plasmoid region to a minimum, the distance between two PD systems is at least 5 cm. The PD systems can be aligned vertically or horizontally by use of appropriate alignment boards (see figure 1). For the horizontal alignment two different configurations are applied, where the lines of sight are either parallel or focused to the plasmoid ascension axis.

6. Spatio-temporal emission using photodiodes

In the following, signals from the PD systems are presented in units of $[\mathrm{ph}/(\mathrm{m}^2\mathrm{s})]$ and constitute the line-integrated emissivity, i.e. the length of the line of sight for the emission at a specific time step is not taken into account for the figures. It is however considered for assessments of radiated power or energy. Moreover, the measured emission is a mean value over the observation cone with a diameter of 5.3 cm in the center of the plasmoid.

6.1. Vertical dynamic

For figure 7 the PD systems were mounted in the vertical configuration and thus the height profiles of the emissions at 313 nm, 656 nm, and 589 nm are given. Comparing the evolutions with high-speed videography shows that for each emission and each height, onset and end of detection is correlated with entering and exiting the LOS and the respective emission time spans are thus a convolution of ascent velocity and the plasmoid size. A decreasing evolution of the intensity with height by several orders of magnitude is common to all emissions, while the gradient depends on the component. During the ascension, the plasmoid's diameter increases from about 10 cm at the time of peak intensity ($t \approx 40$ ms) to about 30 cm at the end of its luminous lifetime. Hence, the varying length of the LOS can be neglected in a first instance compared to the underlying processes changing the emissivity of the plasma by orders of magnitude.

For PD systems at 5 cm it is furthermore to keep in mind that the main plasmoid, or the half-sphere at that time, leaves the LOS after about 40–60 ms (see figure 2) and the remaining detected emission arises from the plasma jet or the transition region. In this height, opening the switch between 150 and 160 ms can thus be seen at a steep decrease of intensity for each emission due to the vanishing plasma channel. Since the plasmoid's ascension is driven by gas dynamics, its evolution at later stages is very sensitive to slight changes of the starting conditions (e.g. increase of
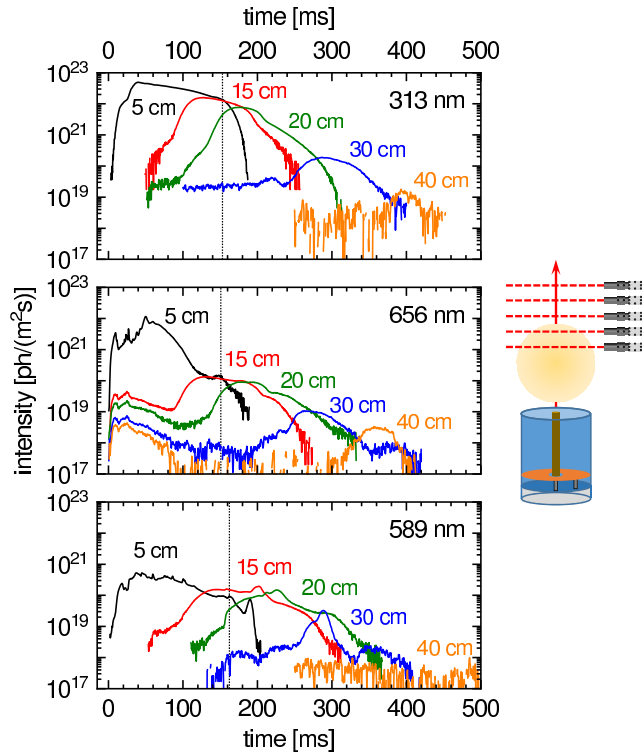
Figure 7. Evolution of the photodiode signals equipped with the 313 nm, 656 nm, and 589 nm filters. Each graph is taken at a single plasmoid discharge, where the five diode systems were mounted vertically to give the respective height profile (in the axis above the central electrode). The dashed line gives the time at which the switch opens in each discharge.

water temperature due to repetitive discharges or the actual water level and degree of wetting of the CE). It should therefore be borne in mind that the reproducibility of emission signals obtained at 30 cm and above might be affected, even if the external parameters are identical.

Signals obtained with the 313 nm filter originate from emission of the OH radical and as already expected from the spectra presented in figure 5, its emission is most intense for nearly the entire plasmoid evolution. From 5 to 40 cm above the water surface it decreases by 3.5 orders of magnitude. Considering the shape and size of the plasmoid from the video frames, an upper limit for the totally emitted radiation via this transition can be estimated: The measured peak intensity in each height is converted to the line emission coefficient in units of $[W/m^3]$ using the respective length of the LOS at that time together with the mean transmitted photon energy of the interference filter ($\approx 4\,eV$) as well as the 50 % detection range. The radiated power density via the entire OH emission can thus be estimated to about $600\,kW/m^3$ in maximum around 40 ms after discharge ignition decreasing to below $0.1\,kW/m^3$ after 400 ms in 40 cm height. To

turn these values into absolute radiated powers, the emitting volume of the plasmoid at the respective times is inferred from the video frames giving about 650 W in maximum and less than 1 W to the end of the evolution. LOS-integration as well as the observation cone give already a reasonable averaging of the emission profiles. The edge emission (vertically as well as horizontally‡), however, is still overrepresented by this analysis, rendering the obtained values upper limits. For a more detailed analysis in this regard a higher spacial resolution (tomography) and a UV-imaging system instead of an optical camera would be required. The time-integrated radiated energy of the entire plasmoid evolution after this analysis would count to about 100 J for the UV range (again as an upper limit).

The 656 nm filter transmits the H_α line emission, but also the continuum radiation which emerges at a later stage (see figure 5). Hence, a discussion of the atomic emission is limited to the first 100 ms and thus to the signal obtained in 5 cm height. However, due to reflections (see section 4) the emission is also detected at 15 cm and above. Comparing the diode signals at 5 cm and 15 cm now shows that the first spectrum in figure 5 underestimates the actual emissivity of atomic species by about two orders of magnitude. Signals obtained with the PD systems in 5 cm height further show that the atomic emission is highly dynamic to the beginning and may even be more intense than the OH emission within the first 10 ms. From $t = 80\,ms$ on, i.e. during the time the plasma jet is recorded in this height, the H_α emissivity starts to decrease rapidly, losing one order of magnitude within 30 ms. The diode signals of the other wavelength ranges do not show such a steep loss of intensity during that time. This drastic time dependence of line ratios (here H_α / OH A-X) is a strong indication for a shift in the equilibrium of the occurring plasma processes within the plasma jet. The maximum emission is obtained between $t = 40$ and 60 ms when the transition region between main plasmoid and jet is in the LOS. Here, about 30 W are emitted via the H_α line (determined as described for the OH emission above) which leads to an upper limit of the total time-integrated emission of about 1 J.

The signals from the PD systems equipped with the 589 nm filters again originate from the sodium line as well as from the continuum. In this case, however, a temporal distinction is not possible, since both emissions emerge at similar times (see figure 5). Hence, specific measures have been undertaken which are described in detail in the next section. The emitted radiation in the wavelength region around 589 nm is less than 2 W in maximum, which makes its influence to the totally radiated energy negligible.

‡ see also section 6.3

In total, the measured values of radiated energy confirm (see [12] for instance) that only a small part ($\approx 3\,\%$) of the total energy delivered to the plasma ($\approx 3.5\,\mathrm{kJ}$) is lost due to radiation in the UV-NIR range. Furthermore, conduction and convection losses of energy are believed to be negligible due to the confining vortex structure. Hence, it is expected that the majority of the input energy is stored in chemical products via endothermic production processes and in their temperature or internal energy (electronic, vibrational and/or rotational excitation). A variety of plasma species—like H, O, OH, H_2O_2, HO_2, O_3, H_3O^+, OH^-, just to name a few—and/or states, in particular metastable states of atomic oxygen, may exist in this atmospheric H_2O plasma, where a multitude of possible processes can lead to production, destruction, population and depopulation (see [23] for instance). Besides electron and heavy particle collisions, radiation trapping can be expected to be of high relevance as well in this expanded atmospheric plasma leading to an expectably high population of even resonance states. In order to gain access to the dominant plasma species and/or states on the one hand and to explain the persisting long-time emission of optical radiation on the other hand, a plasma chemical model is to be developed. Here, the spatio-temporal measurements of the plasma emission can serve as valuable input and benchmark for the model. High-resolution spectroscopy on the OH emission as the dominant emission component will be applied as a next step to determine the vibrational and rotational population of the OH radical and to gain first insights into the occurring plasma processes (see [24] for instance).

6.2. De-ionized water with salt admixtures

In order to discriminate the emission of sodium from the continuum emission at 589 nm the same plasmoid is observed with PD systems equipped with 589 nm and 577 nm filters in the same height. Furthermore, de-ionized water with admixture of NaCl is used, while keeping the conductivity of the water reservoir within the range of standard conditions (see section 2.2). Like this, the sodium content and thus also the share of sodium emission should be increased at else constant external parameters. In addition, a comparison to a discharge using $CaCl_2$ as admixture to de-ionized water is performed as a counterproof. Moreover, also camera 1 was equipped with either a 589 nm or a 577 nm filter to substantiate the findings by visual means. The results are shown in figure 8.

It can be seen in figure 8 (a) that the signals from the PD systems with 589 nm filters and 577 nm filters installed behave quite similar, except for the 589 nm case being slightly more intense during most of the plasmoid evolution. However, shortly after opening the switch a differing behavior can clearly be seen: While the 577 nm signal monotonically decreases, the 589 nm signal shows a strong local maximum about 30 ms after current-zero. This can also be seen in the video frames using the interference filters. At 156.5 ms, directly after shut-down of the discharge current, a cluster emerges at the CE emitting at 589 nm which starts to raise and enters the LOS of the PD system at 5 cm height about 10 ms later. At the time of maximum PD intensity (between 175 and 180 ms) the video image is compared to an equivalent one using the 577 nm filter. The retracting plasma channel is clearly absent in this frame, even with increased contrast. Around 195 ms the ascending cluster can be seen in the signal at 15 cm height and in 30 cm height at 240 ms (frame not shown here). The second maximum in 30 cm height at 320 ms is due to the remaining part of the plasmoid, which has turned to a torus at this stage. In figure 7 this second maximum in 30 cm height is also observable, but due to the lower Na content its intensity is much lower.

Hence, it can be expected that the emission from the plasma channel at 589 nm after opening the switch is mainly correlated to the Na resonance lines and that this emission is responsible for the maxima in the PD signals after current-zero. The counter-evidence is provided by using $CaCl_2$ as the conductivity-imparting salt, shown in figure 8 (b). At the time, where the plasma channel should retract to the main plasmoid no additional emission at 589 nm could be detected and the plasma channel is missing in the video frames even with increased contrast.

It is thus a noteworthy observation, that after current shut-down, the plasma channel does not emit continuum radiation. This constitutes a specific plasma chemistry which is different from the main plasmoid where the continuum radiation is omnipresent. Hence, comparative spectroscopic investigations could provide insight into the origin of the continuum radiation. During the remaining plasmoid evolution, emission from sodium is difficult to distinguish from the continuum radiation when using the PD diagnostic. Further it can be concluded that, as long as Na is present in the water, the ascension of the retracting plasma channel can be monitored at the peaks of the PD signals equipped with 589 nm filters (see for instance also figure 7). Hence, the dynamic of the ascending plasma channel can be distinguished from the dynamic of the main plasmoid. For instance, its ascension velocity is about 5 m/s and thus much higher than the mean velocity of the main plasmoid of 1–2 m/s [15].
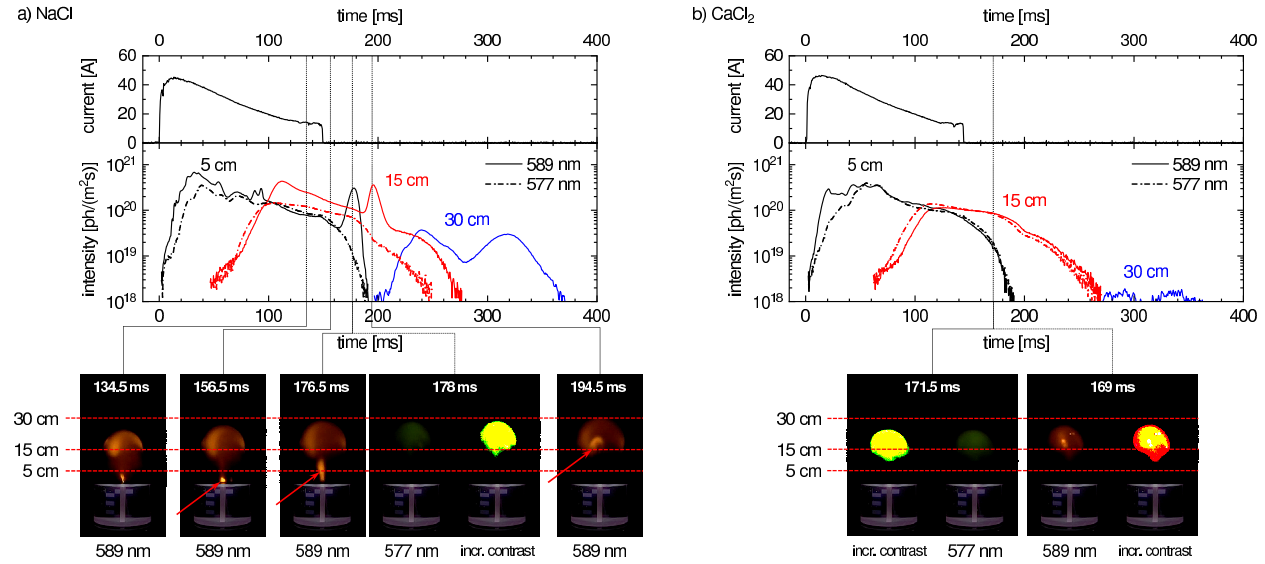
Figure 8. Signals of a plasmoid discharge using de-ionized water with (a) NaCl and (b) CaCl₂ admixture. In 5 cm and 15 cm height, two PD systems were used, one equipped with a 589 nm filter, the other with a 577 nm filter, while in 30 cm only a 589 nm filter was applied. The video camera was also equipped with either a 589 nm or a 577 nm filter. For visibility reasons some of the video frames are increased in contrast here. A depiction of the vessel is added to each of the video frames (not visible in the original videos) to ease perception of the relative plasmoid motion. The arrows in (a) help to recognize an ascending cluster.

6.3. Horizontal structure and symmetry

Using a horizontal alignment of the PD systems, the radial profile of the plasmoid emission as well as its rotational symmetry is investigated. The results are presented in figures 9 and 10. The PD systems are mounted on a retaining plate with a distance of 5.5 cm between each other and the respective LOSs are aligned either parallel to the central PD system or focused to the CE. PD system nr. 5 was, however, not operable during these measurements due to technical issues.

Figure 9 shows the horizontal structure of the H_α and OH emission, the latter for several heights. Emission from the central LOS is thus most intense in 5 cm and 15 cm height, while in 30 cm the turbulent structure of the beginning torus ring formation disturbs this hierarchy for the three central lines of sight. Directly above the water surface in 5 cm height, the central LOS observes the plasma jet while the outer LOSs record the streamers which make up the 'plasma cloud'. The emission is laterally symmetric and the gradients give a declined intensity of 20–50 % within 5 cm down to less than 1 % at the edge of the plasma. However, it is to keep in mind that the length of the LOS is not taken into account for this analysis. For the central LOS the major contribution to the measured signal is expected to come from a very narrow area, namely the plasma jet (see focused frames in figure 2), while the outer LOSs detect an average of the entire plasma cloud with much longer integration length. Gradients of the emissivity, correlated to the density of excited states, will thus be even more peaked. For

15 cm and above the plasmoid spheroid is recorded and here the length of the LOS is decreasing with radial distance and thus the gradients of the emissivity should be flatter than depicted in figure 9. For a more detailed analysis in this regard, the top view videos (camera 2) could be used. However, as can be seen in figure 2, the recordings from this camera are still strongly overexposed during this period. UV transmissive neutral density filters should be applied for that purpose in future.

The rotational symmetry is analyzed by turning the horizontally aligned PD systems such that their lines of sight cross each other at the ascension axis. Figure 10 shows that the emission of atomic hydrogen and OH is rather symmetric within the spanned angle of 32°. Only the dynamic behavior of the atomic emission to the beginning as well as the turbulent behavior at the stage of ring formation slightly disturb the symmetry.

6.4. Variation of energy input

Figure 11 shows the OH emission in 15 cm height for varying energy input. The dissipated energy E is changed between 3.1 and 25.8 kJ by varying the capacitance and the applied voltage and the resulting energy E_{plasma} delivered to the plasma is given in the figure, determined as described in section 3. With increasing energy the intensity of the OH emission increases: a factor 7.5 in energy turns into a factor of 30 in intensity. In addition, the emission starts earlier to rise and simultaneously radiates longer. This
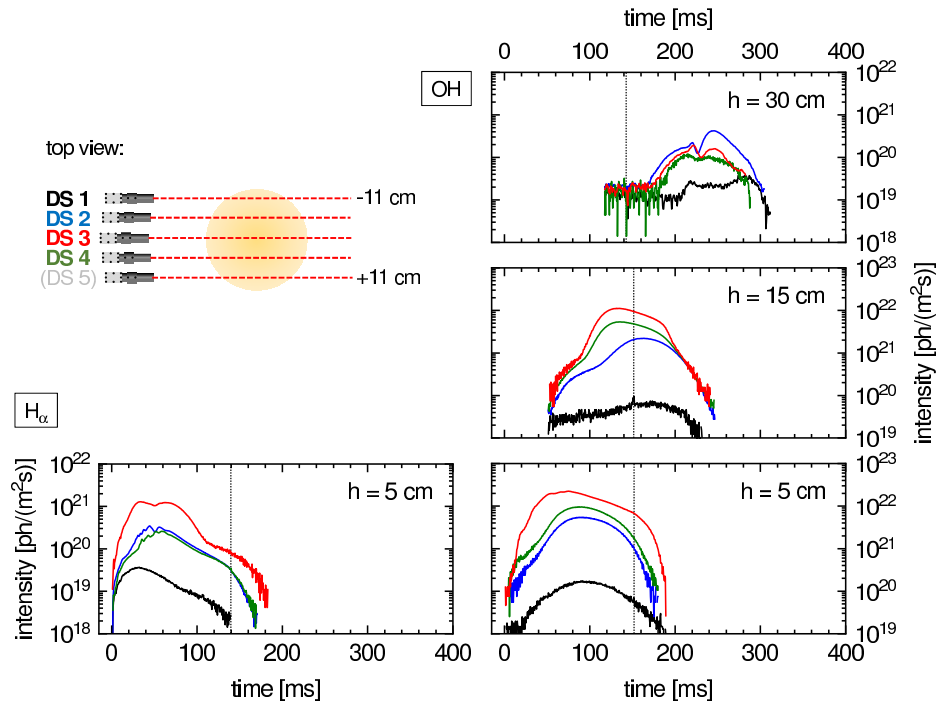
Figure 9. Lateral profiles of the OH and H$_\alpha$ emission in several heights above the water surface. Diode system nr. 5 was not running at that time due to technical issues.
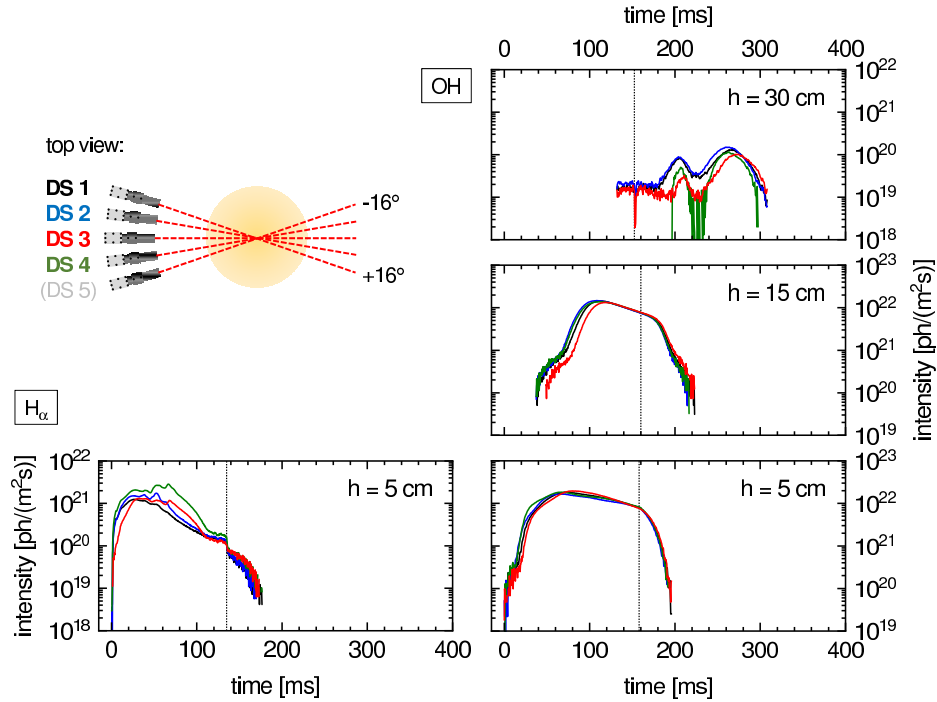

Figure 10. The same as in figure 9 but with a focused alignment of the photodiode systems.

is in accordance with the already shown influence of increasing energy input in [15]: the plasmoid's ascension velocity as well as size increase with energy. This is now impressively confirmed by the spatio-

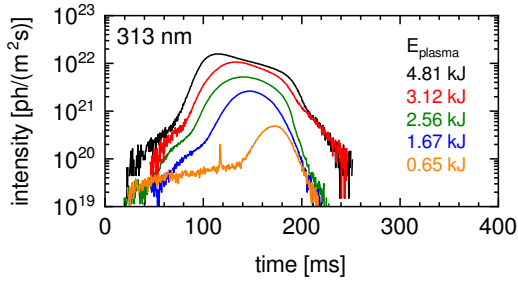temporal emission of OH as it is present at all times.

Figure 11. Evolution of the OH emission in 15 cm height above the water surface for several plasma energies, obtained by varying the capacitance between 0.8 and 2.5 mF and the applied voltage between 2.8 and 5.9 kV.

7. Conclusions

Atmospheric plasmoids generated by a high-voltage discharge above a water surface exhibit an autonomous phase whose origin and the underlying processes are subject of current research. Spatio-temporal investigations of the emitted radiation are a valuable and non-invasive tool to gain insights into this phenomenon. Several high-speed diagnostics including videography and photodiodes are thus applied.

Using a top view camera and an infrared camera it was possible for the first time to prove beyond doubt that the apparently spherical plasmoid turns to a torus ring to the end of its evolution, which is stable for more than 1.5 s. This finding reinforces the hypothesis posed in the literature that the rising plasmoid is actually a vortex from the very beginning. Its visible radiation is terminated after less than 0.8 s. It is illustrated, however, that the exact time strongly depends on the sensitivity of the applied optical camera, which should be borne in mind when comparing 'lifetimes' in the literature. Here, the issue is addressed by using a photodiode together with a reliable mathematical evaluation. Finely timed emission spectra confirm earlier publications in that the main plasmoid is a non-thermal tap-water plasma including emission from the dissolved salts but without influx of ambient air into the plasma. Due to the expected vortex structure, a non-mixing layered system of ambient air and water plasma might additionally be present. Spectroscopic studies of the plasma jet and the streamers above the water surface (plasma cloud) are yet to be done to resolve the difference to published results showing air plasma residues within the plasmoid.

Absolutely calibrated photodiode measurements with high temporal resolution show that the emission from the OH radical dominates nearly the entire plasmoid evolution. Less than 3 % of the total energy used for plasma generation is radiated via this transition and any other optical emission component is negligible for the plasmoid's energy balance. Within the first about 10 ms of the discharge the H_α line intensity 5 cm above the water surface is comparable to or even more intense than the OH emission. Shortly after that, the OH emission increases quickly and dominates the emission henceforth. For all the components the emission is most intense close to the water surface between 40 and 60 ms after discharge ignition, which correlates to the transition region between the forming half-sphere of the plasmoid and the plasma jet connecting it to the CE. In the further course, the emission of the plasma jet (measured at 5 cm height) shows a strong reduction of H_α emission, while the other components only slightly loose intensity. H_α is thus not detected in the main plasmoid in 15 cm height and above. Emission from the dissolved sodium can only be clearly distinguished from the continuum radiation in the retracting plasma channel after current shut-down. Directly above the water surface (5 cm height) the emissions of OH and H_α show a peaked profile in the center due to the plasma jet, while the OH emission from the main plasmoid taken in 15 cm and above shows a broad profile which is laterally and rotationally symmetric for the early phase until about 200 ms.

The omnipresent OH emission of the plasmoid can thus act as a general observable of the plasmoid dynamic. This is demonstrated in a campaign over the variation of the energy input. With increasing energy delivered to the plasma, a larger plasmoid with higher ascent velocity is obtained, which is in accordance with earlier measurements using only videography. The sodium emission, on the other hand, can be applied for monitoring the dynamics of the plasma channel after termination of energy supply, which is used to determine a 4-fold ascension velocity of the retracting channel compared with the main plasmoid.

Next step is the application of finely timed high-resolution spectroscopy at OH to determine the vibrational and rotational population in view of a first identification of relevant excitation and de-excitation processes. Together with the presented spatio-temporal studies using photodiodes, these measurements serve as an input for a chemical model of the atmospheric H_2O plasma. The model is intended to give insight into the dominant plasma processes in order to explain the energy storage mechanisms for the plasmoid's autonomous phase and its prolonged optical emission.

References

[1] Shmatov M L and Stephan K D 2019 *Journal of Atmospheric and Solar-Terrestrial Physics* **195** 105115

[2] Shabanov G D, Krivshich A G, Sokolovskii B Y and Zherebtsov O M 2001 *Proceedings of the 3rd International Conference on Natural and Antropogenetic Aerosols* (St. Petersburg)

[3] Egorov A I and Stepanov S I 2002 *Technical Physics* **47** 1584

[4] Shabanov G D and Sokolovskii B Y 2005 *Plasma Physics Reports* **31** 512

[5] Sakawa Y, Sugiyama K, Tanabe T and More R 2006 *Plasma and Fusion Research* **1** 039

[6] Egorov A I and Stepanov S I 2008 *Technical Physics* **53** 688

[7] Versteegh A, Behringer K, Fantz U, Fussmann G, Jüttner B and Noack S 2008 *Plasma Sources Science and Technology* **17** 024014

[8] Hayashi N, Satomi H, Kajiwara T and Tanabe T 2008 *IEEJ Transactions on Electrical and Electronic Engineering* **3** 731

[9] Hayashi N, Satomi H, Mohri T, Kajiwara T and Tanabe T 2009 *IEEJ Transactions on Electrical and Electronic Engineering* **4** 674

[10] Stephan K D, Dumas S, Komala-Noor L and McMinn J 2013 *Plasma Sources Science and Technology* **22** 025018

[11] Friday D M, Broughton P B, Lee T A, Schutz G A, Betz J N and Lindsay C M 2013 *The Journal of Physical Chemistry A* **117** 9931

[12] Fantz U, Kalafat S, Friedl R and Briefi S 2013 *Journal of Applied Physics* **114** 043302

[13] Fantz U, Briefi S, Friedl R, Kammerloher M, Kolbinger J and Oswald A 2014 *IEEE Transactions on Plasma Science* **42** 2624

[14] Dubowsky S E, Friday D M, Peters K C, Zhao Z, Perry R H and McCall B J 2015 *International Journal of Mass Spectrometry* **376** 39

[15] Fantz U, Friedl R and Briefi S 2015 *Journal of Applied Physics* **117** 173301

[16] Dubowsky S E, Deutsch B, Bhargava R and McCall B J 2016 *Journal of Molecular Spectroscopy* **322** 1

[17] Stelmashuk V and Hoffer P 2017 *IEEE Transactions on Plasma Science* **45** 3160

[18] Versteegh A 2008 Analysis of a long living atmospheric plasmoid Report IPP 13/10 Max-Planck-Institut für Plasmaphysik, Garching

[19] Kalafat S 2012 *Influence of discharge parameters on the physical properties of atmospheric plasmoids* Master thesis Munich University of Applied Sciences in cooperation with University of Augsburg

[20] Stephan K D and Sheleg G 2015 *IEEE Transactions on Plasma Science* **43** 501–505

[21] Sullivan I S, Niemela J J, Hershberger R E, Bolster D and Donnelly R J 2008 *Journal of Fluid Mechanics* **609** 319

[22] Olcay A B and Krueger P S 2008 *Experiments in Fluids* **44** 235

[23] Liu D X, Bruggeman P, Iza F, Rong M Z and Kong M G 2010 *Plasma Sources Science and Technology* **19** 025018

[24] Bruggeman P J, Sadeghi N, Schram D C and Linss V 2014 *Plasma Sources Science and Technology* **23** 023001